



# S-wave velocity structure beneath the High Lava Plains, Oregon, from Rayleigh-wave dispersion inversion

Linda M. Warren<sup>a,\*</sup>, J. Arthur Snoke<sup>b</sup>, David E. James<sup>a</sup>

<sup>a</sup> Department of Terrestrial Magnetism, Carnegie Institution of Washington, 5241 Broad Branch Rd., N.W., Washington, DC 20015, United States

<sup>b</sup> Department of Geosciences, Virginia Polytechnic Institute and State University, 4044 Derring Hall (0420), Blacksburg, VA 24061, United States

## ARTICLE INFO

### Article history:

Received 1 November 2007

Received in revised form 15 April 2008

Accepted 8 July 2008

Available online 20 July 2008

Editor: C.P. Jaupart

### Keywords:

continental intraplate volcanism

Rayleigh waves

High Lava Plains

Oregon

Newberry hotspot track

upper-mantle structure

EarthScope

USArray

## ABSTRACT

The High Lava Plains (HLP) “hotspot” track is a prominent volcanic lineament that extends from the southeast corner of Oregon in the northern Great Basin to Newberry volcano in the eastern Cascades. With the age of silicic volcanism decreasing along track to the northwest, the HLP and Newberry volcano are a rough mirror image to the Eastern Snake River Plain and Yellowstone but, in the case of the HLP, at an orientation strongly oblique to North American plate motion. Since this orientation is incompatible with plate motion over a fixed hotspot, other proposed origins for the HLP, such as asthenospheric inflow around a steepening slab, residual effects of a Columbia River/Steens plume, backarc spreading, and Basin and Range extension, relate it to various tectonic features of the Pacific Northwest. To begin distinguishing between these hypotheses, we image upper-mantle structure beneath the HLP and adjacent tectonic provinces with fundamental-mode Rayleigh waves recorded by stations of the USArray Transportable Array, the recently-initiated HLP seismic experiment, the United States National Seismograph Network, and the Berkeley seismic network. We estimate phase velocities along nearly 300 two-station propagation paths that lie within and adjacent to the HLP and cross the region along two azimuths, parallel to and perpendicular to the HLP track. The dispersion curves, which typically give robust results over the period range 16–171 seconds, are grouped by tectonic region, and the composite curves are inverted for S-wave velocity as a function of depth. We also fit a single plane wave to phase delays across the region to identify laterally homogeneous subregions. The resulting variations in upper-mantle structure correlate with variations in surface volcanism and tectonics. The lowest velocities (~4.1 km/s) occur at ~50 km depth in the SE corner of Oregon, where there has been extensive basaltic volcanism in the past 2–5 kyr, and suggest uppermost mantle temperatures sufficient to produce basaltic partial melting. While the seismic velocities of the uppermost mantle beneath the volcanic High Lava Plains are low relative to the standard Tectonic North America (TNA) model, they are only slightly lower than those found for the adjacent northern Great Basin and they appear to be significantly higher than upper-mantle velocities beneath the Eastern Snake River Plain. Our results provide no evidence for a residual plume signature beneath the HLP region, leaving open questions as to the origin of the HLP volcanic track itself.

Published by Elsevier B.V.

## 1. Introduction

The High Lava Plains (HLP) “hotspot” track is a prominent volcanic lineament that trends southeast–northwest from the southeast corner of Oregon in the northern Great Basin to Newberry volcano in the eastern Cascades (Fig. 1). The HLP and Newberry are a crude mirror image to the Eastern Snake River Plain and Yellowstone (SRP/Y), with the two tracks having a roughly common origin 14–16 Ma in the region of McDermitt Caldera near the western edge of Proterozoic North America in northern Nevada. Silicic volcanism along each chain

becomes progressively younger away from their junction, while primarily basaltic volcanism persists along both tracks. Quaternary volcanic activity in the HLP is concentrated at the ends of the volcanic trends (at Newberry and the Jordan Crater volcanic field). Together, the HLP and SRP/Y represent some of the most volcanically active intraplate regions of North America in the late Cenozoic.

While the direction and age progression of the SRP/Y agree with the trend expected from the motion of the North American plate over a fixed hotspot, the trend of the HLP is oblique to plate motion and therefore inconsistent with a stationary deep mantle source. Other proposed explanations, based on the geology, geochemistry, and geochronology of the surface volcanism, relate the HLP to various tectonic features of the Pacific Northwest. For example, HLP volcanism may be related to Basin and Range extension (Cross and Pilger, 1978). Alternatively, the volcanism may be related in some way to the subduction of the Juan de Fuca plate to the west. Various models for

\* Corresponding author. Tel.: +1 703 292 8722; fax: +1 703 292 9025.

E-mail addresses: [lmwarren@email.arizona.edu](mailto:lmwarren@email.arizona.edu) (L.M. Warren), [snoke@vt.edu](mailto:snoke@vt.edu) (J.A. Snoke), [james@dtm.ciw.edu](mailto:james@dtm.ciw.edu) (D.E. James).

<sup>1</sup> Now at: Department of Geosciences, University of Arizona, 1040 E. 4th St., Tucson, AZ 85721-0077.

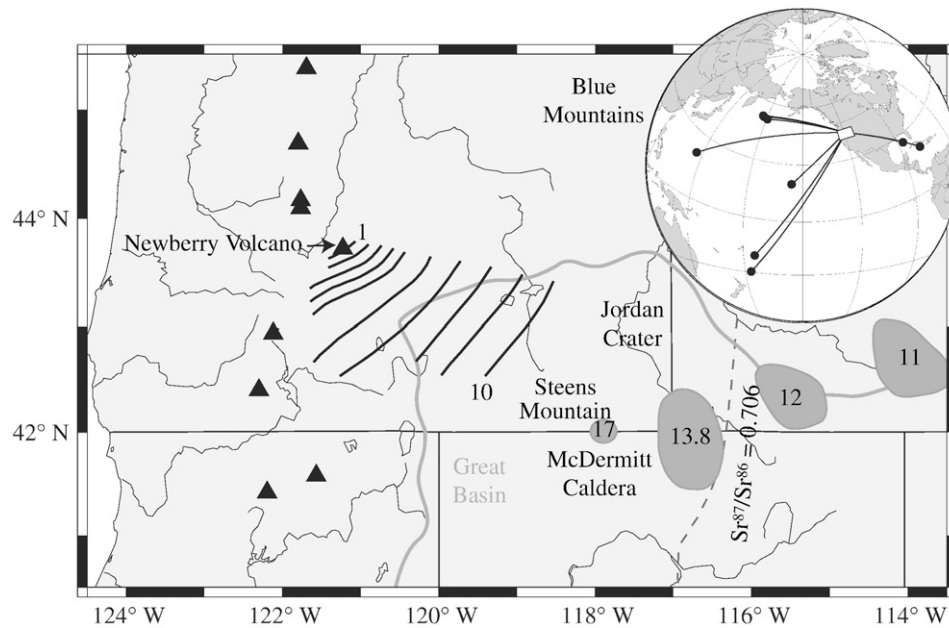


**Fig. 1.** The tectonic setting of the High Lava Plains. Black triangles mark locations of Cascade volcanoes. Black contour lines beginning at Newberry Volcano and extending to the southeast show increasing age of rhyolitic volcanism of the HLP (Jordan et al., 2004). McDermitt Caldera indicates onset of volcanism 16.1 Ma. Dark gray regions show rhyolite calderas along the SRP (Pierce and Morgan, 1992). Gray line outlines the Great Basin (Wernicke, 1992). The dashed  $Sr^{87}/Sr^{86} = 0.706$  line approximates the western boundary of Proterozoic North America (Ernst, 1988). Lower  $Sr^{87}/Sr^{86}$  values lie to the west. The inset shows the geographic setting of the study area and the GCPs to the study area from the analyzed earthquakes (black circles).

the HLP include, for example, back-arc spreading (Christiansen and McKee, 1978) or asthenospheric inflow around a steepening or westerly migrating slab (Carlson and Hart, 1987). One of the more commonly held views on the origin of the HLP relates it to the massive Steens Mountain and Columbia River flood volcanism that began ca. 17 Ma and which immediately preceded both the HLP and SRP/Y hotspot tracks. The flood volcanism has been widely attributed to a plume (e.g. Camp and Ross, 2004), the tail of which is presumed to have produced the SRP/Y volcanism. The plume hypothesis, in addition to encountering immediate problems of plume penetration through a descending slab, also fails to correctly predict key data, notably anisotropy as measured by shear-wave splitting (e.g. Xue and Allen, 2006; Fouch, 2007; Klaus et al., 2007). We are thus left with a number of important questions related to the volcanism of the Pacific Northwest, the most important of which for this study is whether or not a plume is necessary and, if so, what residual plume signature might be observed in the mantle beneath the HLP. Conversely, if large-scale volcanism were a result of back-arc or plate edge effects, would those processes be capable of producing time-dependent focused volcanism as observed in the HLP? Finally, what role, if any, does “topography” at the base of the lithosphere along the boundary of Proterozoic North America play in localizing tectonomagmatism in the overlying crust?

The various HLP scenarios have different implications for crustal basement and upper-mantle seismic structure, but until recently, few data have been available to examine lithospheric structure. This study, based largely on USArray data, is intended to lay a foundation for future studies based on data from a dense array of broadband seismometers being deployed in central and eastern Oregon, southwest Idaho, and northernmost Nevada between 2006 and 2009 as part of a National Science Foundation Continental Dynamics project.

That project, a central component of which is the HLP seismic experiment, will ultimately comprise ~150 broadband seismometers at 10–30 km spacing, sufficient to provide high-resolution images of the uppermost mantle and crust beneath the HLP and adjacent terranes. The broadband array extends ~500 km along strike from the Cascadia arc in the west, across the accreted terranes of eastern

Oregon, and into the Proterozoic lithosphere of the Owyhee Plateau of southwest Idaho and northern Nevada in the east, and ~300 km across strike from the Northern Great Basin in the south to the Blue Mountain Proterozoic terranes in the north. While some very early HLP data were available for this study, most of the data we use are from the USArray Transportable Array (TA) and permanent stations of the United States National Seismograph Network (USNSN) and Berkeley seismic network (see Figure S1).

Data from nine teleseismic earthquakes in the time period February 2006–February 2007 provide a first look at seismic structures that the full HLP experiment will analyze in greater detail. In particular, we image large-scale regional variations in upper-mantle structure by calculating Rayleigh-wave fundamental-mode interstation phase velocities for nearly 300 paths, grouping them by tectonic setting in the region of study, and inverting the regionalized sets for S-wave velocity as a function of depth.

In Sections 2 and 3, we describe our data selection and processing steps and detail our methodology for calculating Rayleigh-wave fundamental-mode phase velocities. In Section 4, we describe the inversion process and present the S-wave velocity models. These models show laterally varying structure in the uppermost mantle within our study area, with the lowest velocities directly beneath the HLP. In the final section, we discuss our results with respect to larger-scale regional structures and, in particular, how they compare to those found for the SRP/Y hotspot track and the adjacent Northern Great Basin.

## 2. Data selection and preparation

Sixteen stations of the HLP deployment were installed in central and eastern Oregon between January and July 2006. The seismometers are broadband, either Streckeisen STS2 or Guralp CMG3T, with RT-130 24-bit data loggers sampling at 40 samples per second (sps). During the same time period, more than 100 broadband stations of the TA were installed in the study area with an average station separation of 70 km. A few permanent stations of the USNSN and the Berkeley seismic network are also located in the region (Figure S1). Not all

**Table 1**

Hypocentral parameters and other information for the analyzed earthquakes. Epicentral distance ( $\Delta$ ) and backazimuth ( $baz$ ) are measured relative to station OR052 (43.52° N, 119.02° W), which is in the middle of the study area

Year:month:day: hour:minute	$M_s$	Latitude	Longitude	Depth (km)	$\Delta$ (km)	$baz$ (°)	$N$	Location
<i>SW–NE-trending paths</i>								
2006:03:31:13:21	6.7	29.61° S	176.83° W	17	10013	227°	42	Kermadec Islands
2006:05:03:15:26	7.9	20.19° S	174.12° W	55	9018	231°	44	Tonga Islands
2006:10:15:17:07	6.7	19.84° N	156.06° W	39	3880	244°	82	Hawaii
<i>NW–SE-trending paths</i>								
2006:02:14:15:27	6.1	20.82° N	146.19° E	40	8816	288°	27	Marianas Islands
2006:06:14:04:18	6.4	51.91° N	177.19° E	14	4771	305°	50	Aleutian Islands
2006:06:27:02:39	6.2	52.11° N	176.22° E	34	4717	305°	60	Aleutian Islands
2006:07:08:20:40	6.6	51.26° N	179.30° W	22	4499	303°	64	Aleutian Islands
2006:09:10:14:56	5.8	23.34° N	86.57° W	10	3491	112°	72	Gulf of Mexico
2007:02:04:20:56	6.1	19.58° N	78.35° W	10	4615	112°	92	Cuba Region

$N$  is the number of stations processed for the event.

stations were in place during the entire period of this study, so different events were recorded by different sets of stations. As indicated in Table 1, the number of stations processed for each event increases with time.

We analyze Rayleigh waves as measured on vertical-component seismograms from all available stations in the study region for nine large, well-recorded earthquakes that occurred in the time interval February 2006–February 2007. The nine analyzed earthquakes have great-circle paths (GCPs) along one of two general azimuths: northwest–southeast and southwest–northeast, approximately parallel to and perpendicular to, respectively, the HLP track. The northwest–southeast-trending paths also contain reverse profiles. Hypocenters of these events are listed in Table 1 and are plotted, along with their GCPs to the study region, in the inset in Fig. 1.

For each earthquake, we process the vertical-component seismograms for all available stations by correcting for the (known) instrument response, decimating to 1 sps, and integrating to displacement. Next, we use a frequency–time analysis (FTAN) (Dziewonski

et al., 1969; Nyman and Landisman, 1977; Levshin et al., 1989) on a representative subset of records to identify the appropriate range of group velocities for each event and to check the quality of the group-velocity spectrum. FTAN results are shown in Fig. 2 for two stations, COR (Corvallis, OR) and N11A (Elko, NV), in different parts of the study area for the 14 June 2006 earthquake in the Aleutians. For both stations, the group-velocity plots are well-behaved from about 16 s to 171 s period, although there are spectral holes near 20 s.

Next, we filter all vertical-component seismograms for each event in both time and frequency. Because our analysis uses correlations and coherence among waveforms, we use the same filtering for all seismograms. The minimum and maximum times are set from the chosen range of group velocities based on examination of FTAN plots from several stations. For the earthquake on 14 June 2006, the chosen group-velocity range is 3.00–3.95 km/s. Hence, at station N11A, with an epicentral distance of 5114 km, the time window is 1295–1705 s.

The time-domain filter is flat over that time window and then is cosine-tapered to zero over a time range of 15% of the selected time window. A similar filter is applied in the frequency domain, with limits of 5 mHz and 60 mHz (200–16.7 s period range). For events with poorer signal-to-noise at long periods, the lower limit may be as high as 8 mHz. Waveforms are padded to 1024 points (1023 s) prior to Fourier transforming to the frequency domain to produce a common set of harmonics.

### 3. Regionalized Rayleigh-wave dispersion measurements

#### 3.1. Selection of station-pairs

Our study area is at an optimum distance from several regions with large earthquakes whose GCPs intersect the continental margin at near-normal incidence and thus produce clean waveforms across the array. For such events, the two-station method, which has a long history (e.g. Sato, 1955; Knopoff, 1972; Kovach, 1978), can be used to obtain estimates of interstation dispersion velocities. In principle, the deconvolution of the near-station waveform from the far-station waveform will remove the effects due to Earth structure between the epicenter and the near station on the calculated dispersions when the two stations are along a common GCP, as well as remove a potential bias due to the focal mechanism. For each pair of stations within the network, we measure the backazimuth from the far station to the epicenter and the backazimuth from the far station to the near station. To ensure GCP propagation, we only use station-pairs for which the difference in backazimuths, which we call  $dbaz$ , is small. While this method is limited

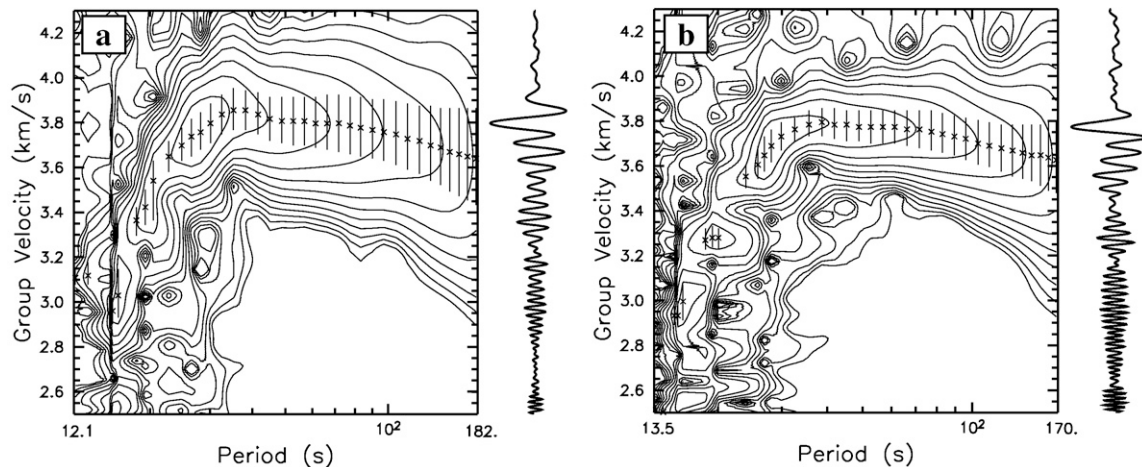


**Fig. 2.** Single-station Rayleigh-wave group velocities vs. period for the earthquake on 14 June 2006 for stations (a) COR ( $\Delta=4366$  km) and (b) N11A ( $\Delta=5114$  km). The instrument-corrected seismogram (shown on the right in each sub-figure) is narrow-bandpass filtered at 34 center frequencies and the quadrature traces (envelopes) are calculated and contoured. The X symbols mark computer-picked quadrature-trace amplitude maxima for each period, and the vertical lines span  $\pm 1$  dB.

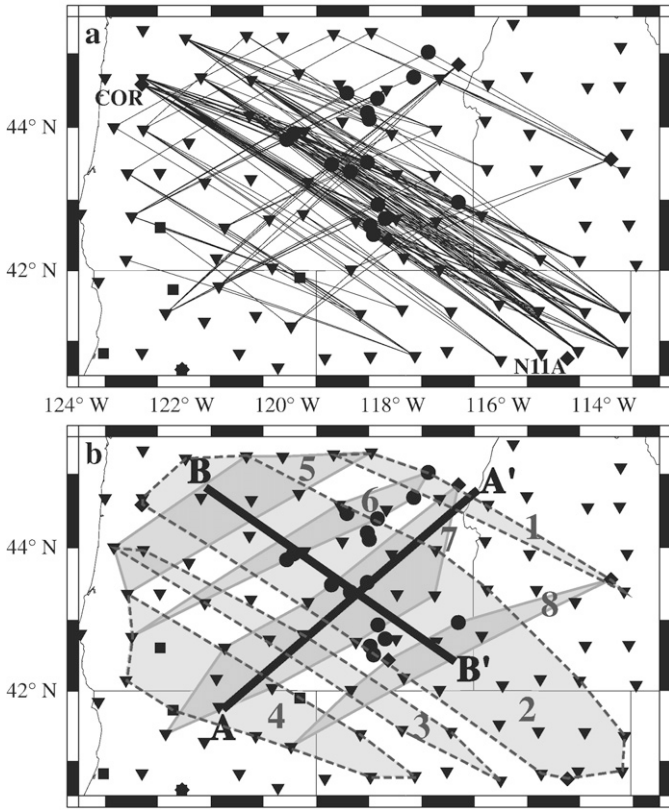


**Fig. 3.** Station locations, GCPs, and regionalized groups. (a) Station locations are plotted as circles (HLP), inverted triangles (USArray/TA), diamonds (USNSN), and squares (Berkeley). The lines connecting stations indicate the two-station GCPs analyzed in this study. Labeled stations COR and N11A are featured in Figs. 2 and 5. (b) The two-station GCPs are divided into eight groups (shaded polygons) by tectonic region. Lines A–A' and B–B' indicate locations of cross-sections in Fig. 8.

by the earthquake and station geometries, the dense network of TA and HLP stations results in many suitable station-pairs. For the nine earthquakes in our study, we identify station-pairs with  $dbaz \leq 3^\circ$  and an interstation distance of  $\geq 200$  km (Fig. 3a, Table S1). This results in 294 station-pairs: 260 pairs with GCPs parallel to the HLP volcanic track, and 34 station-pairs with track-perpendicular GCPs.

### 3.2. Calculation of interstation phase velocities

We use a variant of the method developed by Herrmann (1987) to calculate estimates of interstation phase velocities and phase-velocity errors from vertical-component waveforms for each identified station-pair. Because the method is published only in Herrmann's program notes for *xspcrs*, we present here an expanded version of those notes.

Following the development of Herrmann (1987), define  $X(\omega)$  and  $Y(\omega)$  to be the frequency-domain spectra, for frequency  $\omega$ , for the near station and far station, respectively. Using the difference in epicentral distance of the two stations ( $d$ ) and a reference phase-velocity spectrum ( $c_r(\omega)$ ), the near-station spectrum is time-shifted to the epicentral distance of the far station. This linear phase shift of  $\omega d/c_r(\omega)$  typically removes the need for phase unwrapping in the cross-correlation. For this study,  $c_r(\omega)$  are calculated from a modified version of the Tectonic North America model (Grand and Helmberger, 1984), which we call mTNA and describe later in Section 4.

The autocorrelation and cross-correlation spectra are computed from the relations

$$XX(\omega) = X(\omega)X(\omega)^* \quad (1)$$

$$YY(\omega) = Y(\omega)Y(\omega)^* \quad (2)$$

$$XY(\omega) = X(\omega)Y(\omega)^*, \quad (3)$$

where  $*$  denotes the complex conjugate.

Let  $\Delta\omega$  be the frequency interval ( $\Delta\omega = 2\pi/T$ , where  $T$  is the total duration of the waveforms – 1023 s, in our case) and denote the discrete frequency  $\omega_k = k\Delta\omega$ ,  $k=1, N_f$ , where  $N_f$  is the number of harmonics. Following Jenkins and Watts (1968) and Shumway (1988), we then compute the smoothed spectra  $\overline{XX}$ ,  $\overline{YY}$ , and  $\overline{XY}$  at frequency  $\omega_k = k\Delta\omega$  as

$$\overline{XX}(\omega_k) = \frac{1}{L} \sum_{n=-L/2}^{+L/2} XX(\omega_k + n\Delta\omega), \quad (4)$$

where  $L$  is a positive odd integer. We use similar expressions for  $\overline{YY}$  and  $\overline{XY}$ .

The coherency squared,  $\kappa_{XY}^2(\omega)$ , at each discrete frequency is then given by

$$\kappa_{XY}^2 = \frac{|\overline{XY}|^2}{\overline{XX} \overline{YY}}. \quad (5)$$

The estimated cross spectra are given by

$$H(\omega) = \frac{\overline{XY}}{\overline{XX}} = A(\omega)e^{i\phi(\omega)}, \quad (6)$$

where  $A(\omega)$  and  $\phi(\omega)$  are the amplitude and phase spectra.

Because of the smoothing, we have redundant information that can be used to estimate the confidence on the cross spectra. Defining a factor

$$\Phi(\omega) = \sqrt{\frac{1}{L-1} f_{2,2(L-1)}(1-\alpha)(1-\kappa_{XY}^2 \kappa_{XY}^2(\omega))}, \quad (7)$$

where  $f_{2,2(L-1)}$  is the  $F$ -test statistic, then the  $100(1-\alpha)\%$  confidence intervals on the amplitude and phase spectra are  $A(\omega)(1 \pm \Phi)$  and  $\phi(\omega) \pm \sin^{-1}(\Phi)$ .

The phase velocity ( $c=c(\omega)$ ) and its estimated error ( $\Delta c(\omega)$ ) are then calculated from

$$\frac{1}{c(\omega)} = \frac{1}{c_r(\omega)} - \frac{\phi(\omega)}{\omega d} \quad (8)$$

and

$$\Delta c(\omega) = \frac{c(\omega)^2 \phi(\omega)}{\omega d}. \quad (9)$$

The error bounds,  $\Delta c(\omega)$ , are not derived directly from the dispersion but rather are based on the hypothesis that the two signals – the observed and the model-based propagated waveforms – are the same. The error bound on the phase is projected onto the assumed dispersion with the caveat that the dispersion variation is all due to propagation. (R. B. Herrmann, personal communication, 2008)

The dispersion velocities  $c(\omega_k)$  at discrete frequencies are used to invert for the S-wave velocity structure. The implicit assumption is that each  $c(\omega_k)$  is independent of the others. However, keeping the dispersion at every frequency gives excessive weight to higher frequencies compared to lower frequencies. Thus, based on tests, we selected a set of 15 frequencies/periods that represent approximately equal interdependence across the spectrum. For the reference mTNA model, the sensitivity kernels for the selected periods are shown in Fig. 4. As the phase-velocity coherency calculation is independent for each frequency, we choose to vary  $L$  to be larger at higher frequencies so that there is no overlap in neighboring frequencies used in the

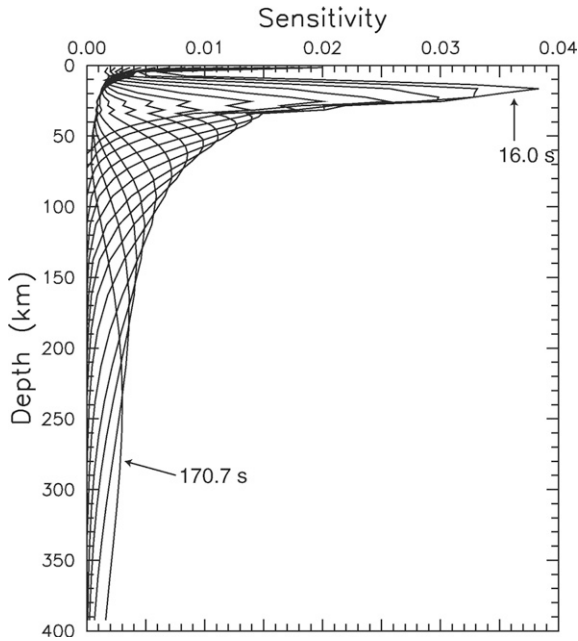


**Fig. 4.** Sensitivity kernels for Rayleigh waves for reference model mTNA at periods of 16.0, 17.7, 19.7, 22.3, 25.0, 28.4, 33.0, 37.9, 44.4, 53.9, 68.5, 85.5, 102.4, 128.0, and 170.7 s, which were used in this study. The curves corresponding to the shortest and longest periods are labeled.

inversion and no gaps in the spectrum. We choose  $L=3$  for the longest period (170.7 s) and  $L=11$  at the highest frequency (16.0 s period).

Fig. 5 shows results of using the coherency procedure to estimate phase velocities for station-pair COR-N11A for three earthquakes in the Aleutian Islands. Note that even though there are spectral holes

**Table 2**  
Tectonic provinces of the regionalized groups

Group number	Orientation	Number of station-pairs	Tectonic provinces
1	NW-SE	6	Blue Mountains, Proterozoic North America
2	NW-SE	218	Primarily High Lava Plains
3	NW-SE	13	Northern Great Basin, HLP, Cascades
4	NW-SE	23	Northern Great Basin, Cascades
5	SW-NE	5	Cascadia
6	SW-NE	8	Cascades, HLP, Blue Mountains
7	SW-NE	16	Northern Great Basin, central HLP, Blue Mountains
8	SW-NE	5	Northern Great Basin, Steens Mountain region (with recent HLP volcanism), Proterozoic North America

the FTAN plots for the waveforms at these stations for the event on 14 June 2006 (Fig. 2), this averaging produces well-behaved phase velocities with small estimated errors down to a period of 16 s. In addition, all three events produce consistent estimates of phase velocities (within the bounds of the estimated errors) even though the waveforms from the events are quite different (Fig. 5b–d).

3.3. Tectonic regionalization

We group the 294 interstation dispersion curves into eight tectonic regions (Table 2, Fig. 3b). For the northwest–southeast-trending GCPs, the groups transition from the Blue Mountains and Proterozoic North America in the northeast (group one), through the HLP province (groups two and three), and into the northern Great Basin (group four). Group two, the axis of which passes along the main trend of the HLP and through the greatest station density, contains substantially more station-pairs than the other groups and accordingly the upper-mantle structure is comparatively well determined. The southwest–northeast-trending GCPs move from Cascadia, in the northwest

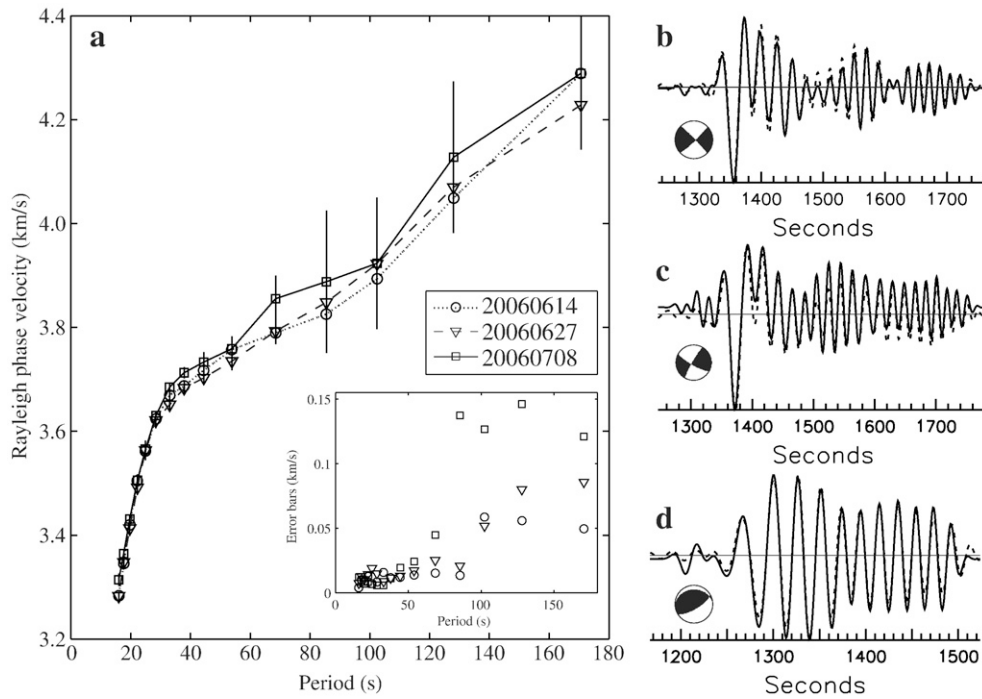
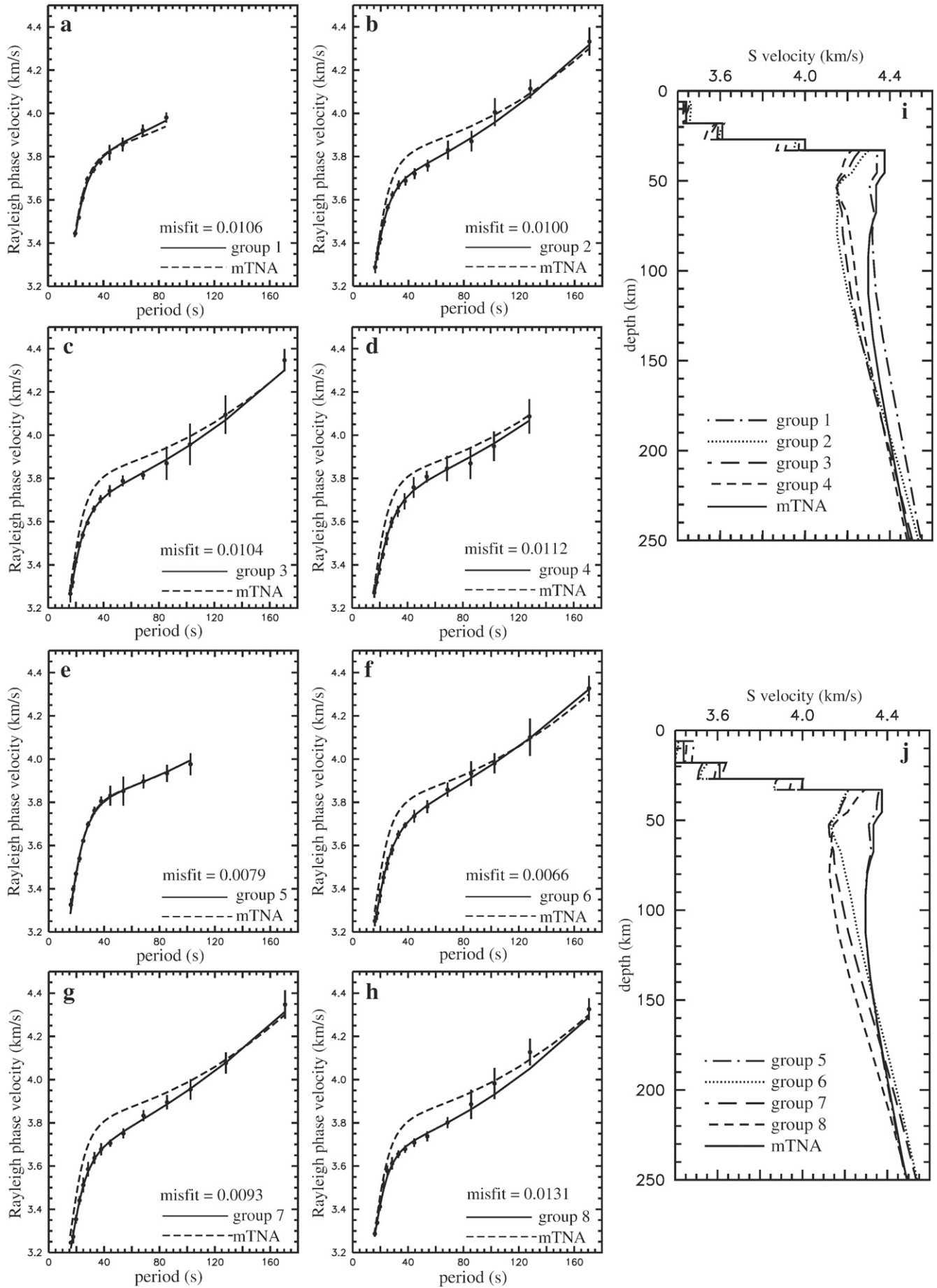


**Fig. 5.** The GCP from COR to N11A is within our backazimuth selection criterion for the three Aleutian Islands earthquakes. All three show consistent estimates of interstation phase velocities (a) even though the waveforms (b–d) for the three events are quite different. (a) Estimated errors (vertical lines) in phase velocity are based on the coherence of the two waveforms. As shown in the inset, error bars are largest for the 8 July 2006 earthquake at periods  $\geq 68$  s. Shown in the right-hand panel are waveforms and focal mechanisms for the (b) 14 June 2006, (c) 27 June 2006, and (d) 8 July 2006 earthquakes. The dotted lines are the time-shifted time series from COR (near station) using the calculated interstation dispersion to correct for the additional epicentral distance. The solid lines are for the (unaltered) N11A waveforms.



(group five), to the HLP and the northern Great Basin (groups six and seven) to the Steens Mountain Region (group eight). Group eight includes the region around Jordan Valley where there has been significant Recent (2–5 kyr) basaltic volcanism.

We combine the dispersion curves into a single composite dispersion curve for each group, weighting the individual phase-velocity values by the inverse of their estimated error. The estimated standard deviation at each frequency of the composite dispersion curve is calculated from the (weighted) dispersion values. As illustrated in Fig. 6a–h, there are significant regional differences among the composite dispersion curves across the study area.

### 3.4. Lateral variations in phase velocity

Fig. 6a–h shows similar phase velocities in the period range 50–90 s for all paths except for the two northernmost ones (groups one and five), where phase velocities are significantly higher. For a dense array of stations (as we have in our study area), two-dimensional residual phase-delay maps are useful for directly imaging such lateral variations. We have developed a method to construct 2D phase-delay maps and apply it to our study area. Our method is similar to the first step of a procedure developed by Forsyth and colleagues (Forsyth et al., 1998; Li et al., 2003; Weeraratne et al., 2003; Forsyth and Li, 2005). The main differences between Forsyth's method and ours include how phase delays are calculated and how the perturbed wavefront is modeled. The details of our method are described in detail in a separate paper (J. A. Snoke, L. M. Warren, and D. E. James, *Determining regional surface-wave phase velocities using coherency and wavefront modeling*, manuscript in preparation). Here we include a brief description of the method as it applies to our dataset.

If the Earth were laterally homogeneous, the wavefronts (equal-time surfaces) would be perpendicular to the epicenter-station GCPs and would be well approximated by planes within the network of recording stations, provided that the network has a lateral extent of less than several hundred kilometers. In the real Earth, heterogeneous structure between the epicenter and network may result in wavefronts entering the study region that are not perpendicular to the GCPs. Both Forsyth's and our modeling techniques assume that such a bending of the wavefront at a fixed frequency can be modeled by solving for a small perturbation to the wavefront. Forsyth's procedure models the incoming wavefield to the study area as the superposition of two plane waves with different amplitudes, directions, and phases. In our method, we treat the incoming wavefield as having a wavefront that can be modeled as a single plane wave, and we solve for a deviation from the GCP of the incoming wavefront. The appropriateness of one vs. two plane waves may be related to the structural complexity between the earthquake and the seismic network. For example, in a study of the East Pacific Rise, Forsyth et al. (1998) found that the waveforms were too complex to be modeled by a single plane wave, so they instead used the superposition of two plane waves. Our high density 2D seismic array allows us to be more selective in our choice of earthquakes and limit the analysis to earthquakes at backazimuths with less potential for multipathing. As a result, as we show below, we find that a single plane wave is sufficient to model the wavefront crossing the HLP.

In both methods, corrections for wavefront perturbations are calculated at fixed frequencies ( $\omega$ ) from phase delays ( $\delta\theta$ ) or, equivalently, time shifts ( $\delta t$ , where  $\delta\theta = \omega\delta t$ ), for arrivals at all stations relative to a reference station. In addition, both methods assume that the study area is laterally homogeneous: the phase velocity calculated

from inversion of observed phase delays at a given period is constant across the study area. Thus, if the study area is homogeneous, contour maps of residual time (or phase) delays will show small residuals. Conversely, if the study area covers a region with significant variations in velocity structure, the structural variations will be apparent in complex spatial patterns in residual time (or phase) delays. Hence, such maps provide a qualitative assessment of homogeneity. 2D residual time-delay maps calculated for different sets of stations within the study area allow the identification of laterally homogeneous subregions and refined estimates of phase velocities within them.

In our method, we apply the coherency procedure described in Section 3.2 to measure the residual time delays for all stations relative to a reference station. At each specified period, we do a nonlinear inversion of the  $\delta t$ s to determine the azimuth of the best-fitting single-plane-wave wavefront and the average phase velocity across the array. If there is no change in the azimuth of the normal to the wavefront, the calculated phase velocity for each station-pair is the differential epicentral distance divided by the time shift from the coherency calculation. If the angular shift is non-zero, the differential distances between stations will not be the same as the difference in GCPs unless the two stations share a common GCP. To date, all measured angular wavefront shifts are at most a few degrees, which is one reason the two-station method with small  $dbaz$  gives robust results.

We apply the wavefront modeling method to waveforms from the 15 October 2006 Hawaii event to examine a large region in the Pacific Northwest that extends from northern California and northern Nevada north to the Canadian border and from the Pacific coast east into Idaho and Nevada. Since we observe the largest differences in phase velocity between the HLP and northern regions between 50 and 90 s (Fig. 6a–h), we choose to perform this analysis at a period of 68.5 s, which is in the middle of this band. Rayleigh waves at 68.5 s period have a maximum sensitivity at  $\sim 90$  km depth (Fig. 4).

First, we model the wavefront using records from 148 stations across the entire region. The contours of observed-minus-predicted time shifts (Fig. 7a) have a complicated pattern with residuals running from  $-2$  s to  $+2$  s, indicating that a single plane wave does not provide a good fit to time shifts. Not surprisingly, we conclude that there are lateral heterogeneities within this extended region.

Because of the high density of TA and HLP stations in our study area, we can subdivide the greater region into smaller subregions based on the results of our regionalized paths and still have enough stations to produce well-constrained inversions. Accordingly, we perform the same analysis procedure for two subregions, one centered on the HLP region (excluding groups one and five) and the other to the north of that region.

For the subregion centered on the HLP, which contains 33 stations, the contours of observed-minus-predicted arrival times (Fig. 7c) show little structure and the range in residual times is less than 2 s. The predicted time shifts are based on a plane wave traveling at  $3.81 \pm 0.04$  km/s with its propagation direction shifted by  $0.5^\circ \pm 1.1^\circ$  counterclockwise from the GCP, a rotation indistinguishable from zero. Phase velocities at this period for the regionalized paths crossing the HLP (groups two through four and six through eight) are in good agreement with phase velocities from the single-plane-wave wavefront modeling.

Because of the shape of groups one and five (Fig. 3b), there are not enough stations to create a well-constrained 2D phase-velocity map restricted to them. Instead, we present results for a subregion to the

**Fig. 6.** Dispersion curves and S-wave velocity models. (a–h) Estimated phase velocities (circles with error bars) for the eight regionalized groups, as identified in the legends. On each plot, the solid line shows the dispersion curve for the best-fitting model based on linearized least-squares with a damping of 10% of the maximum eigenvalue of the data kernel and the dashed line indicates the predicted dispersion curve for the mTNA model. The listed misfit is for the solid curve. For groups one, four, and five the waveforms were not well-constrained at longer periods. The right-hand panels show the best-fitting models of S velocity with depth for the northwest-southeast-trending (i) and southwest-northeast-trending paths (j).

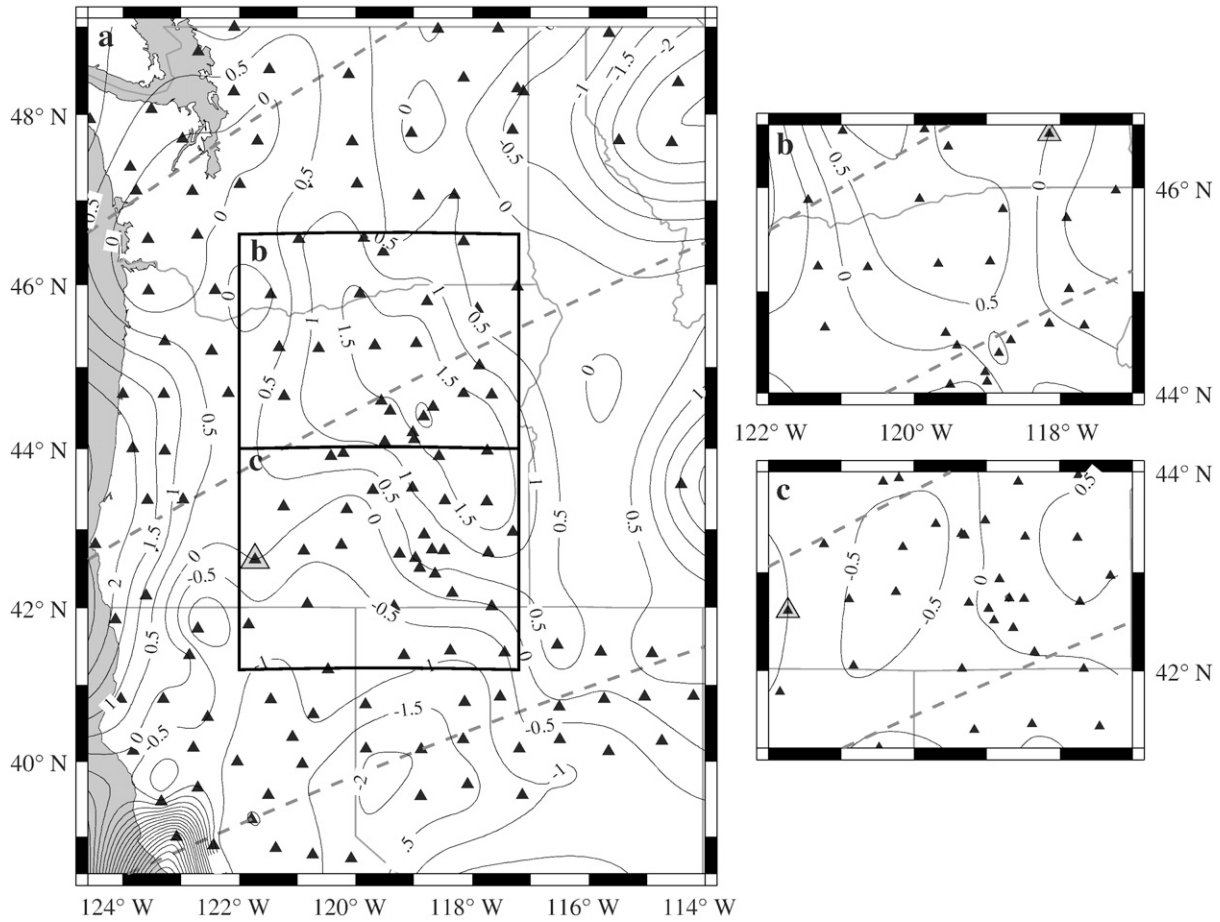


**Fig. 7.** Lateral homogeneity tests using residual phase delays for the 15 October 2006 Hawaii earthquake at 68.5 s period. (a) For a large region around the HLP, the contours of observed-minus-predicted arrival times show distinct patterns in different parts of the study area, indicating that the entire region cannot be fit by a single plane wave. The lack of structure in the contours for smaller regions (b, to the north of the HLP; c, centered on the HLP) indicates that each of those subregions is relatively homogeneous. Black triangles show stations used in the analysis, with the reference station for each model run indicated by a larger gray triangle. Dashed lines show GCPs from the earthquake epicenter. Although the same phase-delay data are used for stations in common among the subregions, each station set is modeled separately.

north of the HLP that includes groups one and five. For this northern subregion (Fig. 7b), which contains 24 stations, the predicted times are based on a plane wave traveling at  $3.89 \pm 0.04$  km/s and shifted by  $1.7^\circ \pm 0.9^\circ$  clockwise from the GCP. Again in this subregion, the lack of structure in the contours of observed-minus-predicted arrival times indicates lateral homogeneity. Although much of this region was not included in the two-station analysis, the statistically significant higher phase velocity at this period is consistent with the results shown in Fig. 6. The difference in phase velocities of the plane waves between this subregion and the HLP subregion, as well as the different incidence angles of the plane waves, confirm the heterogeneity inferred from analysis of the larger region.

#### 4. Surface-wave inversion

We quantify spatial variations in Earth structure by inverting the eight regionalized dispersion curves separately for S-wave velocity as a function of depth following the method described by Snoke and James (1997) and Larson et al. (2006). Larson et al. (2006) performed the inversion in two stages. First, they did a linearized least-squares inversion (LLSI) using program *surf* written by Herrmann (1987). That was followed by a direct-search Neighbourhood Algorithm (NA) inversion (Sambridge, 1999a,b). While the NA method provided error statistics on the model, the LLSI provided a good estimate of the final model. For this preliminary study, we use only the LLSI method. As described in Section 3.2, data for the inversion are the regional phase velocities for the selected set of periods.

We construct a layered starting model, prescribing constant P- and S-wave velocities ( $v_p$ ,  $v_s$ ), attenuation, and density for each layer, down to 650 km depth. For the upper mantle, we use S-wave velocities from the Tectonic North America (TNA) model (Grand and Helmberger, 1984). P-wave velocities, attenuation, and density are taken from AK135 (Kennett et al., 1995), except we use slightly lower values for the P-wave velocity for depths less than 125 km. For the crust, we fix the Moho at 33 km and we use average P-wave velocities from a controlled-source refraction profile beginning at Newberry volcano and extending ~200 km to the east (Catchings and Mooney, 1988). The lowermost crust is taken to have a P-wave velocity of 7.2 km/s. Crustal S-wave velocities are calculated assuming  $v_p/v_s = 1.8$ . Henceforth, we refer to this composite starting model as modified Tectonic North America (mTNA).

Next, we invert the composite dispersion curves for S-wave velocity models as a function of depth using the LLSI methodology of Herrmann (1987). After each iteration, the misfit  $M$  between data and computed dispersion velocities is calculated as

$$M = \sqrt{\frac{\sum_{j=1}^N \left[ \frac{o_j - c_j}{\sigma_j} \right]^2}{\sum_{j=1}^N \left[ \frac{1}{\sigma_j^2} \right]}}, \quad (10)$$

where  $N$  is the number of dispersion velocities,  $o_j$  and  $c_j$  are the observed and calculated values, respectively, for the  $j$ th dispersion

velocity, and  $\sigma_j$  is the estimated standard deviation for  $\sigma_j$ . Note that if the mean of the observed-minus-predicted phase velocities were zero, the definition of misfit would reduce to the standard deviation.

During the inversion, we use differential smoothing (which damps differences between velocities in neighboring layers), and we hold the P-wave velocity, density, and attenuation constant. We decrease the damping parameter (with three to five iterations at each value) until the improvement in misfit is small and the S-wave velocity profile takes on an unphysical shape due to the lack of constraints for the smaller eigenvalues of the data kernel. (See Larson et al. (2006) for further discussion.) The results presented here are all for a damping of 10% of the maximum eigenvalue of the data kernel.

We have tested several different starting models in which we vary the Moho depth and seismic velocities. As expected, there is considerable trade-off between Moho depth and the velocity structure

down to a depth of ~50 km (Figure S2). Because our minimum period is 16 s, we have sensitivity only to the average crustal structure. Data collected by the ongoing HLP and TA deployments will provide more constraints on crustal structure, which is likely to vary significantly across the region (e.g. Das and Nolet, 1998). Since we have limited crustal data at this time, we only interpret velocity variations for depths >50 km. The maximum period of at least 102 s provides constraints on the S-wave velocity structure down to at least 200 km depth. The longest maximum period of 171 s for some regions constrains structure down to >250 km depth.

The LLSI output S-wave velocity models are plotted in Fig. 6i–j and spatially interpreted in Fig. 8. Groups one and five, which are the only two paths not passing through the HLP and Great Basin, are similar to mTNA and have substantially higher velocities in the uppermost mantle than the other subregions. For the other subregions, the lowest

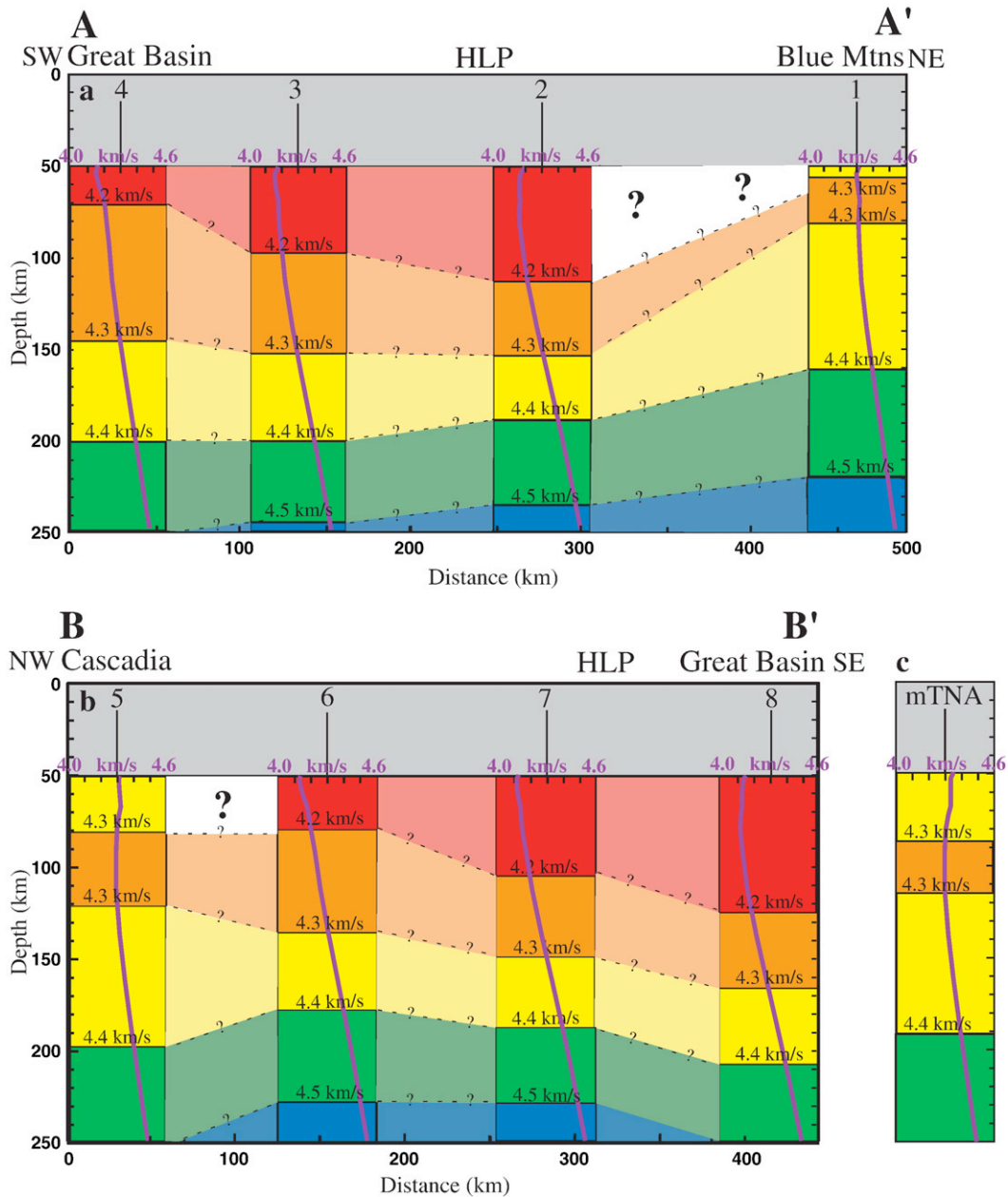


**Fig. 8.** (a and b) Cross-sections interpreting S-wave velocity with depth along lines A–A' and B–B' of Fig. 3b. Velocity profiles for the eight regionalized paths are plotted at the center of the appropriate region and dashed lines with question marks interpolate structure between the regions. The large question marks in two of the transition regions indicate possible discontinuities in structure for which we have no constraints. S-wave velocity structure shallower than 50 km is not interpreted because it trades off with crustal thickness. (c) The velocity–depth profile for the mTNA starting model is shown for comparison.

velocities of  $\sim 4.1$  km/s occur at 50–90 km depth and the low-velocity region (which we define as having  $v_s \leq 4.2$  km/s) extends over the depth range 70–125 km. For the northwest–southeast-trending paths (groups two through four), upper-mantle velocities are lower and the low-velocity region extends to greater depth directly beneath the HLP (group two). To the southwest and into the northern Great Basin (group four) the low-velocity zone tends to be less pronounced for depths greater than  $\sim 60$  km. The southwest–northeast-trending paths show similar variations: the lowest upper-mantle velocities and the broadest low-velocity region are beneath regionalized group eight, where major basaltic flows have occurred over the past few thousand years. To the northwest (groups seven and six), the low-velocity region of mantle is also less pronounced for depths greater than  $\sim 60$  km.

## 5. Discussion

The preliminary surface-wave analyses presented above indicate regional differences in uppermost-mantle structure between the HLP and neighboring tectonic provinces. The lowest upper-mantle velocities are largely confined to the region of the HLP and the northern Great Basin south of the Blue Mountains. With the exception of the Blue Mountains region (group one) and Cascadia (group five), upper-mantle velocities in our study area are considerably lower than those of mTNA. The low-velocity region with the shallowest ( $\sim 50$  km depth) and slowest ( $\sim 4.1$  km/s) velocities is beneath southeastern-most Oregon, a locus of basaltic volcanism over the past several thousand years. The strength and depth extent of the upper-mantle low-velocity zone decreases slightly from the HLP towards the west and south into the northern Great Basin. However, the contrast is small: our phase velocities between 30 and 70 s are only slightly lower than those estimated for paths across the Basin and Range (Koch and Stump, 1996). Looking more broadly across the entire western United States, Yang and Ritzwoller (2008) analyzed TA data with the two-plane-wave method. Within our study region, their phase velocities at 50–100 s are similar to, but typically several hundredths of a km/s lower than, ours.

Upper-mantle velocities beneath the HLP are not as low as those found from similar surface-wave studies of the SRP/Y hotspot track (Schutt et al., 2008). For that region, Schutt et al. (2008) report ultra-low shear velocities, with  $v_s = 3.8 \pm 0.1$  km/s at 80 km depth. These low S-wave velocities were derived from dispersion curves exhibiting phase velocities considerably lower than those measured for the HLP, so the differences cannot be attributed simply to differences in the inversion process and must be real. Body-wave tomography also shows abnormally low P- and S-wave velocities directly beneath the SRP/Y (Saltzer and Humphreys, 1997; Schutt and Humphreys, 2004). The difference in upper-mantle velocity between the HLP and SRP/Y is yet another characteristic, along with gravity signature and surface topography, in which the two volcanic tracks are significantly different. In both cases, however, upper-mantle velocities are sufficiently low as to suggest temperatures sufficiently high to produce regional partial melting. In the case of the HLP, the region of relatively hot upper mantle appears to extend broadly southward into the Northern Great Basin.

The evidence for significantly lower S-wave velocities in the uppermost mantle beneath the SRP/Y (Schutt et al., 2008) relative to the HLP is consistent with differences in volumetric estimates of volcanic products for the two regions. SRP/Y volcanism exceeds that of the HLP by a considerable amount, probably around a factor of ten (R. W. Carlson, personal communication, 2008). Moreover, while the bimodal basalt/rhyolite nature of the volcanism is similar along both SRP/Y and HLP tracks, the voluminous basaltic volcanism of Newberry volcano is dwarfed by the massive silicic volcanism associated with the Yellowstone caldera. In any case, it is clear that high temperatures and large-scale partial melting continue to the present day beneath both the HLP and SRP/Y. The primary cause of high mantle temperatures, particularly beneath the HLP, remains an active topic of ongoing investigations.

While the results presented here are indicative of high temperatures in the uppermost mantle beneath the HLP, we look to future studies using data currently being collected by the full HLP deployment to provide more critical constraints on geodynamical models. In related work, for example, shear-wave splitting results from the initial HLP deployment indicate a remarkably regular pattern, with the fast polarization direction uniformly oriented east–west (Klaus et al., 2007; Fouch, 2007). This orientation is oblique to the age progression of the volcanic track and suggests that, if the fast polarization direction indicates the direction of asthenospheric flow, the asthenosphere is not flowing along the HLP track. We would also expect along-track flow to result in measurable differences between our track-parallel and track-perpendicular S-wave velocity profiles, yet we do not find such azimuthal variations. Regionalized groups two (track-parallel) and seven (track-perpendicular), which both propagate through the middle of the HLP region, display very similar S-wave velocity profiles, suggesting minimal differences in azimuthal velocity variation between the two propagation directions. Moreover, the S-wave velocities shown in this paper are broadly consistent with recent P-wave results obtained from body wave tomography (Roth et al., in press).

A major unresolved issue remains that of evidence for or against a mantle plume beneath the Pacific Northwest. While our HLP results do not provide plausible support for plume interaction, earlier SRP/Y studies do provide ample support for a plume in that region. These and other fundamental problems pertaining to regional tectonomagmatism are currently being pursued with body-wave and surface-wave tomographic analyses, comprehensive anisotropy studies, and geodynamic modeling.

## Acknowledgments

The authors owe a special debt of gratitude to the team of USArray in general and to the project manager, Bob Busby, in particular for the broadband data that have been emerging in real time from the vast rolling Transportable Array deployment. The HLP Project established a much more dense broadband array within the confines of the USArray deployment. The project is the work of a large team of scientists across the spectrum of geology, geochemistry, and geophysics. Details can be found at <http://www.dtm.ciw.edu/research/HLP/>. We wish to thank first and foremost Jenda Johnson – without her help in obtaining station permits, this project would have been difficult indeed. The seismic experiment would have been impossible without the extraordinary cooperation, hospitality, and outright assistance of ranchers and other landowners throughout the HLP region who have freely hosted seismic stations on their land. Special appreciation is due the Eastern Oregon Agricultural Research Center/Agricultural Research Service and our many friends there who have provided invaluable office facilities and many other resources for this experiment. The seismic component of the project was made possible by the efforts of students, postdocs and PIs, seismologists and otherwise. Significant contributors to the HLP field deployment include: ASU PI Matthew Fouch; ASU graduate students Jeff Roth, Kevin Eagar, John West, Lauren Mattatall, Angela Magee, and Shaji Nair; ASU post-doctoral fellow Caroline Beghein; Carnegie PI Richard Carlson; Carnegie postdoctoral fellows Catherine Cooper and Maureen Long; OSU students David Trench, Mark Ford, Mike Iademarco, and Tom Wagner; Oklahoma University's Steve Holloway. Special appreciation goes to Steven Golden, the able Carnegie field seismologist, for contributions to the field effort and for managing all data submissions to the IRIS DMC. This project, USArray, and HLP would not have been possible without the help of the extraordinarily able personnel of the PASSCAL Instrument Center. As always, we thank the highly efficient staffs of PASSCAL and the IRIS Data Management Center who archived and distributed the data collected by this experiment. This manuscript benefited from discussions with Lara Wagner and Matt Fouch, and

constructive comments from three anonymous reviewers, Matt Fouch, and Rick Carlson. Funding for the HLP Project was provided by U.S. National Science Foundation (NSF) award EAR-0506914. LMW was supported by NSF and a Harry Oscar Wood Postdoctoral Fellowship while at the Carnegie Institution.

## Appendix A. Supplementary data

Supplementary data associated with this article can be found, in the online version, at doi:10.1016/j.epsl.2008.07.014.

## References

- Camp, V.E., Ross, M.E., 2004. Mantle dynamics and genesis of mafic magmatism in the intermontane Pacific Northwest. *J. Geophys. Res.* 109, B08204. doi:10.1029/2003JB002838.
- Carlson, R.W., Hart, W.K., 1987. Crustal genesis on the Oregon Plateau. *J. Geophys. Res.* 92, 6191–6206.
- Catchings, R.D., Mooney, W.D., 1988. Crustal structure of east central Oregon: relation between Newberry volcano and regional crustal structure. *J. Geophys. Res.* 93, 10,081–10,094.
- Christiansen, R.L., McKee, E.H., 1978. Late Cenozoic volcanic and tectonic evolution of the Great Basin and Columbia Intermontane regions. In: Smith, R.B., Eaton, G.P. (Eds.), *Geol. Soc. Amer. Mem.*, pp. 283–311.
- Cross, T.A., Pilger, R.H., 1978. Constraints on absolute motion and plate interaction inferred from Cenozoic igneous activity in the western United States. *Am. J. Sci.* 278, 865–902.
- Das, T., Nolet, G., 1998. Crustal thickness map of the western United States by partitioned waveform inversion. *J. Geophys. Res.* 103, 30,021–30,038.
- Dziewonski, A., Block, S., Landisman, M., 1969. A technique for analysis of transient seismic signals. *Bull. Seismol. Soc. Am.* 59, 427–444.
- Ernst, W.G., 1988. Metamorphic terranes, isotopic provinces, and implications for crustal growth of the western United States. *J. Geophys. Res.* 93, 7634–7642.
- Forsyth, D.W., Li, A., 2005. Array-analysis of two-dimensional variations in surface wave velocity and azimuthal anisotropy in the presence of multipathing interference. In: Levander, A., Nolet, G. (Eds.), *Seismic Data Analysis and Imaging with Global and Local Arrays*. Geophys. Monogr. AGU, Washington, D.C., pp. 81–98.
- Forsyth, D.W., Webb, S.C., Dorman, L.M., Shen, Y., 1998. Phase velocities of Rayleigh waves in the MELT experiment on the East Pacific Rise. *Science* 281, 1235–1238.
- Fouch, M.J., 2007. Asthenospheric dynamics of the Pacific Northwestern United States. EarthScope National Meeting, Monterey, CA.
- Grand, S.P., Helmlinger, D.V., 1984. Upper mantle shear structure of North America. *Geophys. J. R. Astron. Soc.* 76, 399–438.
- Herrmann, R.B., 1987. *Computer Programs in Seismology*. St. Louis University, St. Louis, Missouri.
- Jenkins, G.M., Watts, D.G., 1968. *Spectral Analysis and Its Applications*. Holden-Day, San Francisco. Chapter 10.
- Jordan, B.T., Grunder, A.L., Duncan, R.A., Deino, A.L., 2004. Geochronology of age-progressive volcanism of the Oregon High Lava Plains: implications for the plume interpretation of Yellowstone. *J. Geophys. Res.* 109, B10202. doi:10.1029/2003JB002776.
- Kennett, B.L.N., Engdahl, E.R., Buland, R., 1995. Constraints on seismic velocities in the Earth from travel times. *Geophys. J. Int.* 122, 108–124.
- Klaus, A., Wagner, L.S., Long, M.D., James, D.E., 2007. Shear-wave splitting and seismic anisotropy in Oregon's High Lava Plains. *Eos Trans. AGU, Fall Meet. Suppl.* 88 (52) Abstract S41B-0560.
- Knopoff, L., 1972. Observation and inversion of surface-wave dispersion. *Tectonophysics*, 13, 497–519.
- Koch, K., Stump, B.W., 1996. Constraints for upper mantle shear-wave models of the Basin and Range from surface-wave inversion. *Bull. Seis. Soc. Am.* 86, 1591–1607.
- Kovach, R.L., 1978. Seismic surface waves and crustal and upper mantle structure. *Rev. Geophys. Space Phys.* 16, 1–13.
- Larson, A.M., Snoke, J.A., James, D.E., 2006. S-wave velocity structure, mantle xenoliths and the upper mantle beneath the Kaapvaal craton. *Geophys. J. Int.* 167, 171–186.
- Levshin, A.L., Yanovskaya, T.B., Lander, A.V., Bukchin, B.G., Barmin, M.P., Ramikova, L.L., Its, E.N., 1989. Surface waves in vertically inhomogeneous media. In: Keilis-Borok, V.I. (Ed.), *Surface Waves in a Laterally Inhomogeneous Earth*, pp. 131–182.
- Li, A., Forsyth, D.W., Fischer, K.M., 2003. Shear velocity structure and azimuthal anisotropy beneath eastern North America from Rayleigh wave inversion. *J. Geophys. Res.* 108, 2362. doi:10.1029/2002JB002273.
- Nyman, D.C., Landisman, M., 1977. The display-equalized filter for frequency-time analysis. *Bull. Seis. Soc. Am.* 67, 393–404.
- Pierce, K.L., Morgan, L.A., 1992. The track of the Yellowstone hotspot: volcanism, faulting, and uplift. In: Link, K., Kuntz, M.A., Platt, L.B. (Eds.), *Regional Geology of Eastern Idaho and Western Wyoming*. Mem. Geol. Soc. Am., vol. 179, pp. 1–53.
- Roth, J.B., Fouch, M.J., James, D.E., Carlson, R.W., High Lava Plains Seismic Working Group, 3-D seismic velocity structure of the northwestern United States, in press. *Geophys. Res. Lett.*
- Saltzer, R.L., Humphreys, E.D., 1997. Upper mantle P wave velocity structure of the eastern Snake River Plain and its relationship to geodynamic models of the region. *J. Geophys. Res.* 102, 11,829–11,841.
- Sambridge, M., 1999a. Geophysical inversion with a neighbourhood algorithm I: searching a parameter space. *Geophys. J. Int.* 138, 479–494.
- Sambridge, M., 1999b. Geophysical inversion with a neighborhood algorithm II: appraising the ensemble. *Geophys. J. Int.* 138, 727–746.
- Sato, Y., 1955. Analysis of dispersed surface waves by means of Fourier Transform: Part 1. *Bull. Earthq. Res. Tokyo Univ.* 33, 33–47.
- Schutt, D.L., Humphreys, E.D., 2004. P and S wave velocity and vp/vs in the wake of the Yellowstone hot spot. *J. Geophys. Res.* 109, B01305. doi:10.1029/2003JB002442.
- Schutt, D.L., Dueker, K., Yuan, H., 2008. Crust and upper mantle velocity structure of the Yellowstone hotspot and surroundings. *J. Geophys. Res.* 113, B03310. doi:10.1029/2007JB005109.
- Shumway, R.H., 1988. *Applied Statistical Time Series Analysis*. Prentice-Hall, Englewood Cliffs. Chapter 2.
- Snoke, J.A., James, D.E., 1997. Lithospheric structure of the Chaco and Paraná Basins of South America from surface-wave inversion. *J. Geophys. Res.* 102, 2939–2951.
- Weeraratne, D.S., Forsyth, D.W., Fischer, K.M., 2003. Evidence for an upper mantle plume beneath the Tanzanian craton from Rayleigh wave tomography. *J. Geophys. Res.* 108, 2427. doi:10.1029/2002JB002273.
- Wernicke, B., 1992. Cenozoic extensional tectonics of the U.S. Cordillera. In: Burchfiel, B.C., Lipman, P.W., Zoback, M.L. (Eds.), *The Geology of North America*, vol. G3, The Cordilleran Orogen: Conterminous United States. Geol. Soc. Amer., pp. 553–581.
- Xue, M., Allen, R.M., 2006. Origin of the Newberry hotspot track: evidence from shear-wave splitting. *Earth Planet. Sci. Lett.* 244, 315–322.
- Yang, Y., Ritzwoller, M.H., 2008. Teleseismic surface wave tomography in the western U. S. using the Transportable Array component of USArray. *Geophys. Res. Lett.* 35, L04308. doi:10.1029/2007GL032278.